

# **Forschungsartikel**



Single-Atom Catalysis

Zitierweise: Angew. Chem. Int. Ed. 2024, 63, e202410457 doi.org/10.1002/anie.202410457

# **Subsurface Single-Atom Catalyst Enabled by Mechanochemical Synthesis for Oxidation Chemistry**

Xuze Guan, Rong Han, Hiroyuki Asakura,\* Bolun Wang, Lu Chen, Jay Hon Cheung Yan, Shaoliang Guan, Luke Keenan, Shusaku Hayama, Matthijs A. van Spronsen, Georg Held, Jie Zhang, Hao Gu, Yifei Ren, Lun Zhang, Zhangyi Yao, Yujiang Zhu, Anna Regoutz, Tsunehiro Tanaka, Yuzheng Guo,\* and Feng Ryan Wang\*

**Abstract:** Single-atom catalysts have garnered significant attention due to their exceptional atom utilization and unique properties. However, the practical application of these catalysts is often impeded by challenges such as sintering-induced instability and poisoning of isolated atoms due to strong gas adsorption. In this study, we employed the mechanochemical method to insert single Cu atoms into the subsurface of Fe<sub>2</sub>O<sub>3</sub> support. By manipulating the location of single atoms at the surface or subsurface, catalysts with distinct adsorption properties and reaction mechanisms can be achieved. It was observed that the subsurface Cu single atoms in Fe<sub>2</sub>O<sub>3</sub> remained isolated under both oxidation and reduction environments, whereas surface Cu single atoms on Fe<sub>2</sub>O<sub>3</sub> experienced sintering under reduction conditions. The unique properties of these subsurface single-atom catalysts call for innovations and new understandings in catalyst design.

#### Introduction

Single-atom catalysts<sup>[1]</sup> (SACs) have received significant attention due to their high atom utilization and unique properties.<sup>[1-2]</sup> SACs show great potential in various applications, including CO oxidation,<sup>[3]</sup> hydrogenation,<sup>[4]</sup> organic reactions,<sup>[5]</sup> as well as electrocatalytic<sup>[6,7]</sup> and photocatalytic reactions.<sup>[8]</sup> The catalytic performance of isolated metal atoms is determined by their locations on supports and the associated coordination environment,<sup>[9]</sup> with current efforts mainly focused on developing surface single-atom catalysts. However, their application is often limited by poor stability resulting from sintering<sup>[10]</sup> and the poisoning of isolated atoms by strong adsorption of impurity gases.<sup>[11]</sup> In this regard, tuning the local atomic configuration is a promising method for achieving stable and enhanced catalytic performance.

Ammonia (NH<sub>3</sub>) plays a crucial role in the selective catalytic reduction (NH<sub>3</sub>–SCR) process, which is used to reduce harmful nitrogen oxide (NO<sub>x</sub>) emissions from diesel vehicle exhaust and power plants.<sup>[12]</sup> However, in SCR systems, excess NH<sub>3</sub> is needed, where NH<sub>3</sub> is not fully utilized and is released into the environment. Selective catalytic oxidation of ammonia (NH<sub>3</sub>–SCO) is one of the most promising methods to remove NH<sub>3</sub> from the exhaust

[\*] X. Guan, Dr. L. Chen, J. H. C. Yan, Dr. J. Zhang, H. Gu, Y. Ren, L. Zhang, Z. Yao, Dr. F. R. Wang

Department of Chemical Engineering, University College London London WC1E 7JE (UK)

E-mail: ryan.wang@ucl.ac.uk

R. Han, Dr. Y. Guo

School of Electrical Engineering and Automation

Wuhan University, Wuhan, 430072, China

E-mail: yguo@whu.edu.cn

Dr. H. Asakura

Department of Applied Chemistry, Faculty of Science and Engineering

Kindai University, 3-4-1, Kowakae, Higashi-Osaka, Osaka, 577-8502, Japan

E-mail: asakura@apch.kindai.ac.jp

Dr. H. Asakura, Prof. T. Tanaka

Department of Molecular Engineering, Graduate School of Engineering

Kyoto University, Kyotodaigaku Katsura, Nishikyo-Ku, Kyoto 615-8510, Japan

Dr. B. Wang

Max-Planck-Institut für Kohlenforschung

Kaiser-Wilhelm-Platz 1, D-45470 Mülheim an der Ruhr, Germany

Dr. S. Guar

Maxwell Centre, Cavendish Laboratory

Cambridge CB3 0HE, UK

Dr. L. Keenan, Dr. S. Hayama, Dr. M. A. van Spronsen, Prof. G. Held

Diamond Light Source Ltd

Harwell Science and Innovation Campus

Didcot, Oxfordshire OX11 0DE (UK)

Y. Zhu, Dr. A. Regoutz

Department of Chemistry, University College London

20 Gordon Street, London WC1H 0AJ, UK

© 2024 The Authors. Angewandte Chemie published by Wiley-VCH GmbH. This is an open access article under the terms of the Creative Commons Attribution License, which permits use, distribution and reproduction in any medium, provided the original work is properly cited.

Angew. Chem. 2024, 136, e202410457 (1 of 10)

© 2024 The Authors. Angewandte Chemie published by Wiley-VCH GmbH

2014/1977, 2024, 42, Downloaded from https://onlinelibrary.wiley.com/doi/10.1002/ange.202410457 by University College London UCL Library Services, Wiley Online Library on [1003/2025]. See the Terms and Conditions (https://onlinelibrary.wiley.com/erens-and-conditions) on Wiley Online Library for rules of use; OA articles are governed by the applicable Creative Commons



gas, which will play a crucial role in the upcoming EU7 standard.[13] The diesel exhaust generally has a temperature of 500 to 700°C at 100% load and normally discharges at a temperature of around 420°C.[14] In the downstream NH3-SCO process following NH3-SCR, high-performance catalysts are essential to achieve complete conversion of NH<sub>3</sub> to N<sub>2</sub> and water (H<sub>2</sub>O), particularly at low temperatures (T < 400°C).

Noble metals supported on metal oxides have been widely recognized for their high catalytic activity in NH<sub>3</sub> oxidation at low temperatures.<sup>[15]</sup> However, a major challenge associated with these catalysts is the tendency for over-oxidation, leading to the formation of nitrogen oxides.[16] To replace noble metals, the development of transition metal catalysts with excellent low-temperature activity and good stability has become a central topic in NH<sub>3</sub>-SCO. However, even the more selective options among these catalysts, such as Cu, have not exhibited sufficient activity to be practically viable.<sup>[17]</sup> In recent years, iron oxide (Fe<sub>2</sub>O<sub>3</sub>) has been proposed as a promising material for deNOx applications, due to its superior performance in medium- and high-temperature ranges (> 300 °C) and good SO<sub>2</sub> resistance in the NH<sub>3</sub>-SCR reaction. [18] Kang et al.<sup>[19]</sup> achieved selective activation of oxygen by employing a cerium (Ce) cation framework to reduce the energy of 3d orbitals of isolated copper (Cu) sites. In our previous study, [20] it was observed that the presence of atomic Cu-O-Fe enhances NH<sub>3</sub> conversion on Fe<sub>2</sub>O<sub>3</sub> surfaces. Remarkably, with the lowest 1s→3d transition energy, atomic Cu-O-Fe achieves a twofold increase in NH<sub>3</sub> conversion in comparison to CuO clusters at 573 K. Furthermore, it maintains high N<sub>2</sub> selectivity at 673 K under conditions involving an inlet NH3 concentration of 5000 ppm. Cu single atoms over Fe<sub>2</sub>O<sub>3</sub> can achieve high NH<sub>3</sub> conversion and N<sub>2</sub> selectivity simultaneously at high temperatures, while the low-temperature activity was much poorer than that of noble-metal catalysts.

Here, we inserted single Cu atoms into the subsurface of Fe<sub>2</sub>O<sub>3</sub> support via the mechanochemical method. [21] The subsurface single atom reveals remarkably different dynamics and adsorption behaviours under reaction conditions. Subsurface Cu sites in the lattice created O vacancies, facilitating the activation of oxygen and redox of surface Fe<sub>2</sub>O<sub>3</sub>. Compared with surface Cu single atoms, subsurface Cu single atoms exhibited high resistance against sintering and resilience to NO poisoning. Additionally, the subsurface Cu atoms remained dispersed under both oxidizing and reducing environments at high temperatures, yielding 100 % NH<sub>3</sub> conversion at 513 K, which is 3.7 times higher than that of surface Cu atoms catalysts. These results provide a new strategy for the rational design of active and stable singleatom catalysts for practical applications. The ability to control the location of single atoms via simple mechanochemical methods highlights the potential of this subsurface single-atom catalyst.

#### **Results and Discussion**

The fresh and surface CuO-Fe<sub>2</sub>O<sub>3</sub> catalyst was prepared by the coprecipitation method with 1 wt % Cu. Subsequently, the Cu single atoms were incorporated into the subsurface via ball milling, as depicted in Figure 1a. Microwave plasmaatomic absorption spectroscopy (MP-AES) confirmed that the Cu ratio of the ball-milled catalyst was similar to that in the fresh catalyst (Figure S1). Due to the similar atomic numbers of Cu and Fe, it is not possible to observe Cu atoms on the Fe<sub>2</sub>O<sub>3</sub> support in STEM. Energy-dispersive Xray spectroscopy (EDX) mappings showed that Cu species were homogeneously dispersed in both fresh and ball-milled samples (Figure 1b, Figures S2 and S3). Extended X-ray absorption fine structure (EXAFS) spectra further demonstrated atomically dispersed Cu, with no evidence of a Cu-Cu scattering path in the spectra of both fresh and ballmilled samples (Figure 1c, fitting results in Figure S4 and Table S1). To distinguish Cu-Fe from Cu-Cu, we applied continuous Cauchy wavelet analysis (CCWT) to the k2weighted EXAFS spectra (Figure S5 and Supporting Note 1), since CCWT has proven to be a very useful tool for obtaining structural information from complex systems.[22] An increase in the coordination number of Cu-Fe (from 2.2 to 2.7, Table S1) implied that Cu single atoms penetrated the interior of the Fe<sub>2</sub>O<sub>3</sub>.

Surface-sensitive X-ray photoelectron spectroscopy (XPS; Figures S6 and S7) revealed the presence of Cu in the fresh catalyst, but could not detect a clear Cu signal in the ball-milled catalyst, indicating that the isolated Cu atoms were not located on the surface of Fe<sub>2</sub>O<sub>3</sub>. The inelastic mean free path (IMFP) of Cu 2p<sub>3/2</sub> electrons in a matrix of Fe<sub>2</sub>O<sub>3</sub> copper is 1.3 nm as calculated using the TPP-2M model. [23] Near edge X-ray absorption fine structures (NEXAFS) spectra for Cu L-edge were measured using both total electron yield (TEY) and Auger electron yield (AEY). TEY provides information about chemical environments with depth sensitivities of 2-5 nm, while AEY is more surfacesensitive and provides information within 1 nm.<sup>[24]</sup> The AEY (Figure 1d) could not effectively detect the Cu signal for the ball-milled catalyst, while the TEY (Figure 1e) showed the presence of Cu in the deeper region. The difference between AEY and TEY suggests that Cu was not present on the surface of Fe<sub>2</sub>O<sub>3</sub> but was located in the subsurface after ball milling, consistent with the XPS and EXAFS results. These findings confirm that the surface Cu single atoms can be inserted into the subsurface of Fe<sub>2</sub>O<sub>3</sub> support through ball milling. To further confirm the position of subsurface Cu in Fe<sub>2</sub>O<sub>3</sub>, the formation energies were calculated to determine the doping sites of the Cu atom in Fe<sub>2</sub>O<sub>3</sub>, and the replacement of Fe atoms is a stable structure (Figure S8 and Supporting Note 2).

The physical adsorption showed that the surface area of the catalyst decreased after ball milling (Figure S9), which could be attributed to pore collapse. X-ray diffraction (XRD; Figure S10) patterns of both fresh CuO-Fe<sub>2</sub>O<sub>3</sub> catalyst and ball-milled catalyst showed an ordered α-Fe<sub>2</sub>O<sub>3</sub> phase. The half-peak width of the ball-milled CuO-Fe<sub>2</sub>O<sub>3</sub> increased, indicating a smaller crystalline domain after ball-

221,42,52 Downloaded from https://onlinelibrary.wiley.com/doi/10.1002/ange.202410457 by University College London UCL Library Services, Wiley Online Library on [1003/2025]. See the Terms and Conditions (https://onlinelibrary.wiley.com/erens-and-conditions) on Wiley Online Library for rules of use; OA articles are governed by the applicable Century on [1003/2025]. See the Terms and Conditions (https://onlinelibrary.wiley.com/erens-and-conditions) on Wiley Online Library for rules of use; OA articles are governed by the applicable Century on [1003/2025]. See the Terms and Conditions (https://onlinelibrary.wiley.com/erens-and-conditions) on Wiley Online Library for rules of use; OA articles are governed by the applicable Century on [1003/2025].

2-5 nm Cu TEY

950

940

Photon energy (eV)

Figure 1. Synthetic Scheme and ex situ characterizations of catalysts. a, Schematic illustration of immersing Cu into Fe<sub>2</sub>O<sub>3</sub> via ball milling. b, Scanning transmission electron microscopy image and the corresponding energy-dispersive X-ray spectroscopy elemental mapping images of Fe  $K\alpha_1$ , Cu  $K\alpha_1$  and the reconstructed Cu + Fe composition. **c**, Fourier transform of  $k^2$ -weighted EXAFS spectrum of the as-synthesized 1 wt% CuO-Fe<sub>2</sub>O<sub>3</sub> (coprecipitation), 1 wt% CuO-Fe<sub>2</sub>O<sub>3</sub> (ball milling) catalysts and CuO standard. d, Cu L<sub>3</sub> edge NEXAFS AEY spectra. e, Cu L<sub>3</sub> edge NEXAFS TEY spectra.

940

Photon energy (eV)

2 nm Cu AEY

950

milling. High-angle annular dark-field imaging scanning transmission electron microscopy (HAADF-STEM) confirmed that the particles became smaller after ball milling for both Fe<sub>2</sub>O<sub>3</sub> and CuO-Fe<sub>2</sub>O<sub>3</sub> catalysts (Figures S11-S14). Overall, the results demonstrate that Cu single sites were homogeneously dispersed over the Fe<sub>2</sub>O<sub>3</sub> support, and that ball milling was effective in incorporating these single atoms into the subsurface.

R (Å)

Surface oxygen vacancies are a common structural feature resulting from the reductive reconstruction of iron oxide catalysts. Additionally, hydroxyl groups serve as important intermediates in reactions involving H<sub>2</sub>O, H<sub>2</sub>, and hydrocarbons that are catalysed by iron oxide. The ballmilled catalyst has the highest content of adsorbed O species, even higher than the H<sub>2</sub>-activated catalyst (Figure S7b), which is due to the strong adsorption of H<sub>2</sub>O on the surface of defected oxides.<sup>[25]</sup> These results suggest that the surface Fe<sub>2</sub>O<sub>3</sub> undergoes reconstruction during the ball milling process.

930

The structure of subsurface single-atom catalysts (SACs) differs from that of doped metal oxides. For doped metal oxides, the doping elements are evenly distributed in the catalyst, including on the surface. In comparison, for subsurface single-atom catalysts, the single atoms are located beneath the surface. As a result, the active sites for doped metal oxides are usually in the form of M<sub>A</sub>-O-M<sub>B</sub>, while such interfaces are not exposed on the surface for subsurface single-atom. Based on our NEXAFS results, the depth of subsurface Cu species is around 1-5 nm, and their unique position influences their interaction with the surface. This positioning allows them to contribute significantly to the catalytic activity due to their accessibility and modification of surfaces.

The NH<sub>3</sub> oxidation activity of the ball-milled CuO-Fe<sub>2</sub>O<sub>3</sub> catalyst was compared with other samples.

15213737, 2024, 42, Downloaded from https://onlinelibrary.wiley.com/doi/10.1002/ange.202140457 by University College London UCL Library Services, Wiley Online Library on [1003/2025], See the Terms and Conditions (https://onlinelibrary.wiley.com/erms-and-conditions) on Wiley Online Library for rules of use, OA articles are governed by the applicable Centwise.

Fresh catalyst (surface Cu SAC) and ball-milled catalyst (subsurface Cu SAC) were investigated under realistic NH<sub>3</sub> slip conditions (1000 ppm NH<sub>3</sub>, weight hourly space velocity (WHSV) of  $120 \text{ ml}_{\text{NH3}} \cdot \text{h}^{-1} \cdot \text{g}^{-1}$ ). The subsurface Cu SAC shifts the conversion profile 80 K towards the low-temperature region and NH3 is completely converted at 513 K (Figure 2a). After evaluating NH<sub>3</sub>-SCO performance at a higher NH<sub>3</sub> concentration (5000 ppm NH<sub>3</sub>, WHSV of 600 ml<sub>NH3</sub>·h<sup>-1</sup>·g<sup>-1</sup>), the subsurface Cu SAC showed similar N<sub>2</sub> yield with Pt-Al<sub>2</sub>O<sub>3</sub> catalyst from 473 K to 673 K (Figures S15 and S16). At 573 K, the subsurface Cu SAC exhibited the highest N2 yield (Figure 2b), with 5.6 times and 2.4 times improvement relative to the Fe<sub>2</sub>O<sub>3</sub> and surface Cu SAC, respectively. Compared to other catalyst systems in the literature, the 1 wt % CuO-Fe<sub>2</sub>O<sub>3</sub> (ball milling) catalyst achieved the highest N2 productivity of Cu-based catalysts (Figure S17). Additionally, the subsurface Cu SAC even outperformed most noble metal catalysts regarding N2 productivity, N2 selectivity, WHSV, the temperature of full conversion and stability (Figure S18). The subsurface Cu SAC was also found to be stable under a WHSV of  $1200 \text{ ml}_{\text{NH}3} \cdot \text{h}^{-1} \cdot \text{g}^{-1}$  conditions at 573 K, with good stability over a 100-hour testing period (Figure S19).

The internal selective catalytic reduction (i-SCR) mechanism is widely accepted for transition metal catalysts. [15,17a] This mechanism includes two steps. First, NH $_3$  is oxidized to NO (Eq. 1). Then, the unreacted NH $_3$  reacts with as-formed NO to produce N $_2$  (Eq. 2). Compared with noble metals,

transition metals generally show lower catalytic activity due to the slow oxidation rates in step 1. The key aspect in this reaction is the activation of  $O_2$ .

Step 1: 
$$4NH_3 + 5O_2 \rightarrow 4NO + 6H_2O$$
 (1)

Step 2: 
$$4NO + 4NH_3 + O_2 \rightarrow 4N_2 + 6H_2O$$
 (2)

The NH<sub>3</sub> oxidation kinetics exhibited a lower apparent activation energy for the subsurface Cu SAC (~45 kJ mol<sup>-1</sup>, Figure 2c) in comparison with that of the surface Cu SAC (~76 kJ mol<sup>-1</sup>). Moreover, the subsurface Cu SAC exhibited a lower reaction order in  $O_2$  (+0.01 versus +0.62) and a higher reaction order in NH<sub>3</sub> (+0.51 versus -0.26) (Figure 2d,e). The negative order in NH<sub>3</sub> and positive order in O2 of surface Cu SAC catalyst are consistent with the Langmuir-Hinshelwood (L-H)kinetics, [10c,26] in which NH3 or intermediate NO poisoning inhibits the adsorption and activation of O2. In contrast to the fresh catalyst, the O2 order of ~0 for the subsurface Cu SAC suggests more facile oxygen activation. [10c,27] The positive NH<sub>3</sub> order indicates that subsurface Cu single atoms are not poisoned by NH<sub>3</sub> and NO during NH<sub>3</sub> oxidation. These results imply a different mechanism for the subsurface Cu SAC, suggesting that variations in the location of single atoms significantly influence the surface structure and adsorption behaviours.

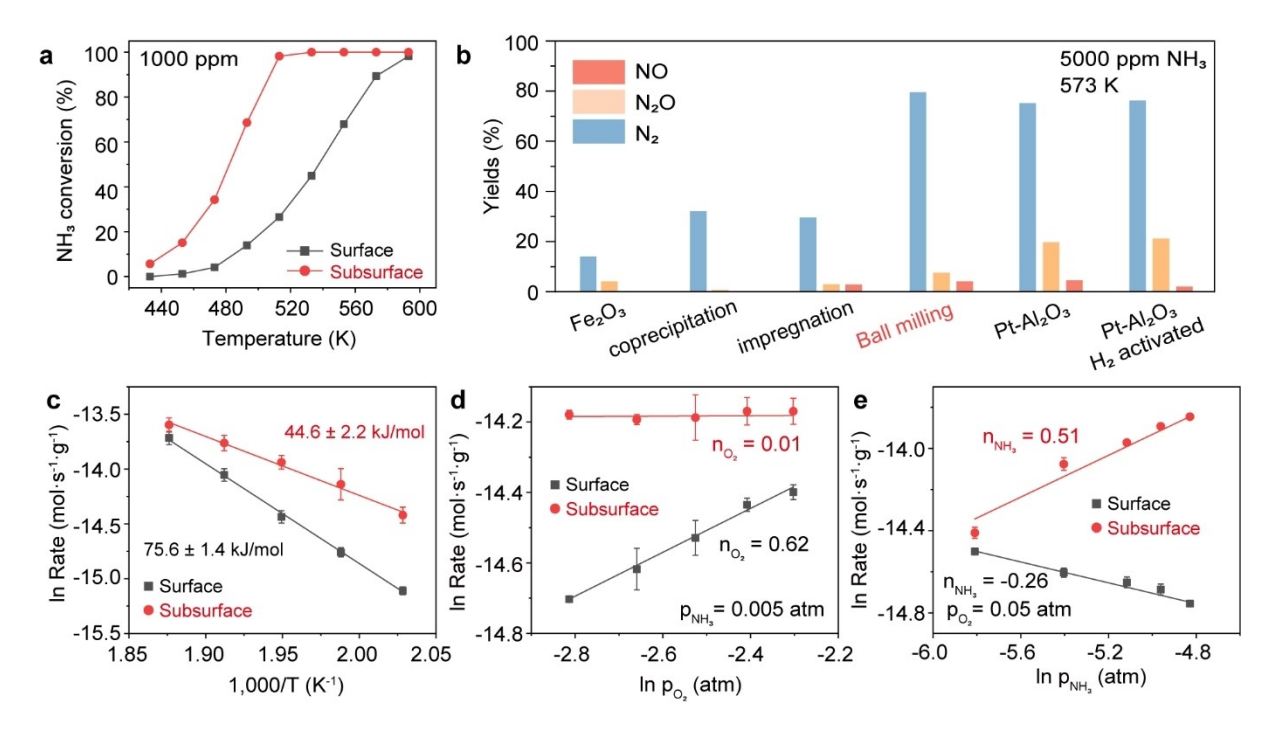


Figure 2. Catalytic reactivity of Cu with different coordination environments. **a**, Steady-state NH<sub>3</sub> conversion plots (1000 ppm NH<sub>3</sub>, 5% O<sub>2</sub>, He balance, and WHSV of 120 ml<sub>NH3</sub>·h<sup>-1</sup>·g<sup>-1</sup>). **b**, Yields of N<sub>2</sub>, N<sub>2</sub>O and NO for various catalysts at 573 K (5000 ppm NH<sub>3</sub>, 5% O<sub>2</sub>, He balance, and WHSV of 600 ml<sub>NH3</sub>·h<sup>-1</sup>·g<sup>-1</sup>). **c**, Arrhenius-type plots for NH<sub>3</sub> oxidation over the fresh sample (surface Cu SAC) and the ball-milled sample (subsurface Cu SAC), where a difference in the 1000/T scale should be noted. **d**, Reaction rate as a function of the O<sub>2</sub> partial pressure measured at 493 K. **e**, Reaction rate as a function of the NH<sub>3</sub> partial pressure measured at 493 K. Reaction orders are estimated as slopes of the linear fit. The data points and error bars represent the average and standard deviation based on multiple measurements on the same catalyst at different times during the experiment.

2024/04, 42, Downloaded from https://onlinelibhary.wiley.com/doi/10.1002/ange.2024/0457 by University College London UCL Library Services, Wiley Online Library on [1003/2025]. See the Terms and Conditions (https://onlinelibnary.wiley.com/erens-and-conditions) on Wiley Online Library for rules of use; OA articles are governed by the applicable Century on [1003/2025]. See the Terms and Conditions (https://onlinelibnary.wiley.com/erens-and-conditions) on Wiley Online Library for rules of use; OA articles are governed by the applicable Century on [1003/2025]. See the Terms and Conditions (https://onlinelibnary.wiley.com/erens-and-conditions) on Wiley Online Library for rules of use; OA articles are governed by the applicable Century on [1003/2025]. See the Terms and Conditions (https://onlinelibnary.wiley.com/erens-and-conditions) on Wiley Online Library for rules of use; OA articles are governed by the applicable Century on [1003/2025]. See the Terms and Conditions (https://onlinelibnary.wiley.com/erens-and-conditions) on Wiley Online Library for rules of use; OA articles are governed by the applicable Century on [1003/2025]. See the Terms and Conditions (https://onlinelibnary.wiley.com/erens-and-conditions) on Wiley Online Library for rules of use; OA articles are governed by the applicable Century on [1003/2025]. See the Terms and Conditions (https://onlinelibnary.wiley.com/erens-and-conditions) on [1003/2025]. See the Term

To confirm the importance of subsurface Cu atoms, we loaded Cu species on the surface of ball-milled Fe<sub>2</sub>O<sub>3</sub> by impregnation. After the addition of 1 wt % Cu on the surface, the ball-milled Fe<sub>2</sub>O<sub>3</sub> shows an increase in the activity (Figure S20). In our previous study, it is found that the bridging O<sup>2-</sup> of Cu–O-Fe has a lower antibonding orbital energy and thus weaker Cu-O/Fe-O strength. In selective NH<sub>3</sub> oxidation, the weak Cu-O/Fe-O bond enables fast Cu redox for NH<sub>3</sub> conversion. However, the NH<sub>3</sub> conversion is still lower than the ball-milled Cu-Fe<sub>2</sub>O<sub>3</sub> catalysts. These results further support the hypothesis that the weak adsorption of NO for subsurface Cu atoms and oxygen vacancies are crucial for enhancing the catalytic activity.

The zero-order dependence on O2 partial pressure in the subsurface Cu SAC suggests that O2 dissociation is not the rate-limiting step. The positive ammonia reaction order for the subsurface Cu SAC points to the Mars-van Krevelen (MvK) mechanism, in which O<sub>2</sub> activation proceeds at the O vacancies of the catalyst<sup>[28]</sup> (Figure 3a). Reducibility is a key feature of oxide catalysts that follow the MvK mechanism in oxidation reactions. A typical description of oxide reducibility is the cost of oxygen vacancy formation, which measures the tendency of the oxide to lose oxygen or donate it to the adsorbed species.<sup>[29]</sup>

Using near-ambient pressure (NAP)-NEXAFS, we measured the reducibility of the catalyst surface. The spectra of the O K-edge demonstrate transitions from the O-1s state to unoccupied states. The hybridized O 2p-Fe 3d levels exhibit predominantly 3d character and are split into  $t_{2g}$  and

e<sub>g</sub> states at 530.7 eV and 532.1 eV (Figure 3b), respectively. With the increasing temperature in the NH<sub>3</sub> atmosphere, the  $t_{2g}$  and  $e_g$  double-peak splitting of ball-milled 1 wt % CuO-Fe<sub>2</sub>O<sub>3</sub> (subsurface Cu SAC) becomes less pronounced, while fresh 1 wt % CuO-Fe<sub>2</sub>O<sub>3</sub> (surface Cu SAC) remains essentially unchanged. The line shape observed in the present ball-milled sample at 573 K suggests the presence of Fe<sub>3</sub>O<sub>4</sub> crystal symmetry. [30] This can be further confirmed by the Fe L<sub>3</sub>-edge NAP-NEXAFS, as shown in Figure 3c. The increased peak of the L<sub>3</sub> peak at lower energy can be assigned to the formation of Fe2+ in the ball-milled catalyst,[31] while the fresh catalyst keeps unchanged from 373 K to 573 K under 1 mbar NH<sub>3</sub> (Figure S21). These results suggest the enhanced redox behaviour of surface Fe after ball milling.

To verify the role of subsurface Cu single atoms, we also measured the O K-edge of ball-milled Fe<sub>2</sub>O<sub>3</sub>. The ballmilled Fe<sub>2</sub>O<sub>3</sub> shows similar reducibility to the fresh CuO-Fe<sub>2</sub>O<sub>3</sub> catalysts, showing no significant reduction under NH<sub>3</sub> at 573 K (Figure S22 and Supporting Note 3). These results confirm that the surface Fe<sub>2</sub>O<sub>3</sub> with Cu in the subsurface is prone to reduction, while the surface Fe<sub>2</sub>O<sub>3</sub> with Cu on the surface keeps stable under NH<sub>3</sub> at 573 K. From this perspective, the subsurface Cu SAC has different active sites from the surface Cu SAC, suggesting variations in the local structure of single-atom catalysts influence the reaction mechanism.

The X-ray absorption near-edge structure (XANES) spectra showed that Cu species in the ball-milled sample are

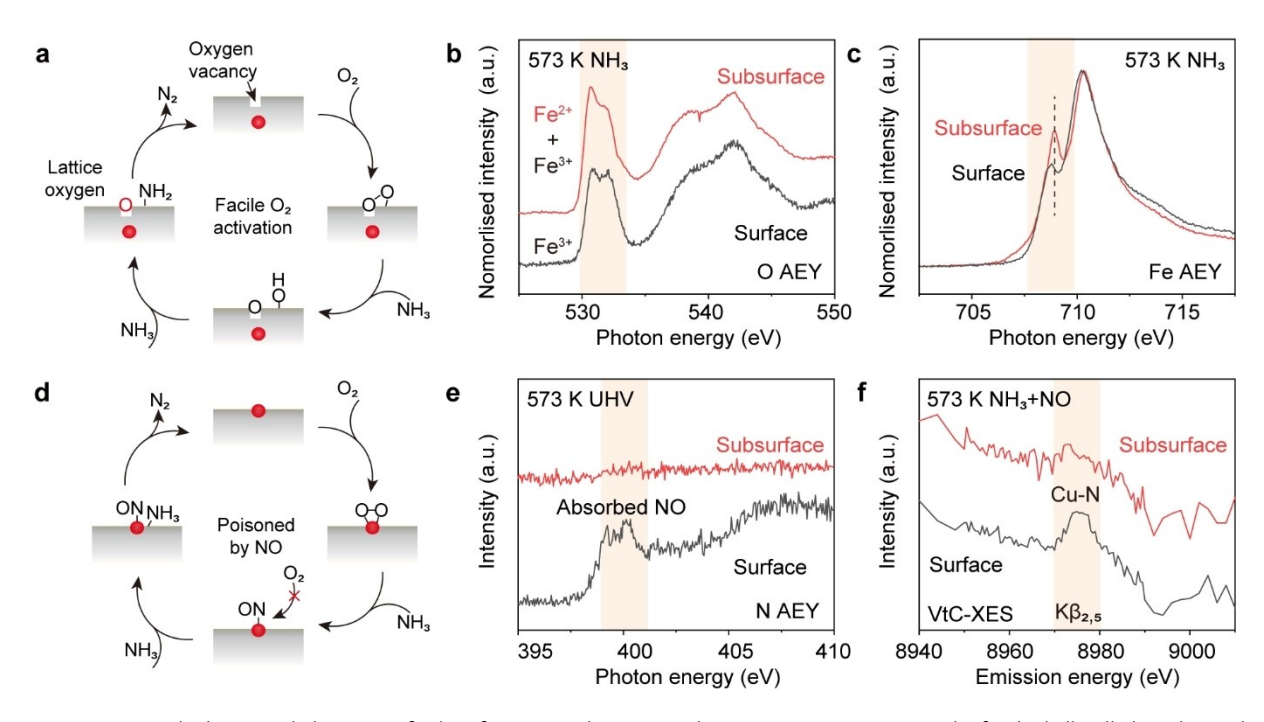


Figure 3. Structure and adsorption behaviours of subsurface Cu single-atom catalyst. a, MvK type reaction paths for the ball-milled catalyst with subsurface Cu single atoms. b, O-K edge NAP-NEXAFS of the fresh catalyst (surface Cu SAC) and the ball-milled catalyst (subsurface Cu SAC) under 1 mbar NH3 at 573 K. c, Fe-L3 edge NAP-NEXAFS of the fresh catalyst (surface Cu SAC) and the ball-milled catalyst (subsurface Cu SAC) under 1 mbar NH1 at 573 K. d, L-H type reaction paths for the fresh catalyst with surface Cu single atoms. e, N K-edge (AEY mode) under UHV at 573 K after adsorption of NO at room temperature. f, VtC-XES spectra of ball-milled catalyst (top) and fresh catalyst (bottom) under NH3+NO at 573 K. Due to the adsorption of Fe and low Cu concentration of the catalysts, the obtained spectra were much nosier.



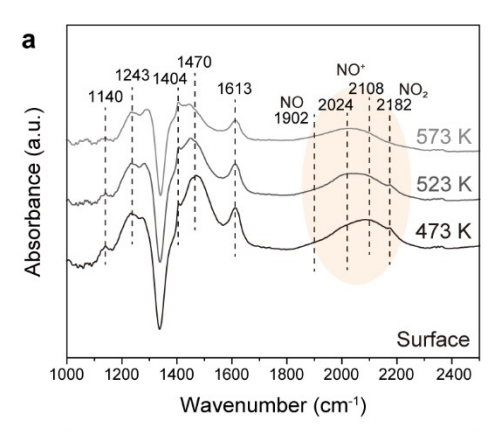
in the oxidation state of +1 and +2, while Cu in the fresh sample is in the form of  $Cu^{2+}$  (Figure S23a). Both catalysts have similar  $1s\rightarrow 4p$  transition energy for  $Cu^{2+}$ , which is higher than that of the CuO standard (Figure S23b). This can be explained by the electron-withdrawing effect of Fe.<sup>[19–20]</sup> Compared with the surface Cu SAC, the subsurface Cu SAC has decreased Cu–O coordination (from 3.2 to 2.6, Table S1), indicating the formation of O vacancy in the catalyst.

Adsorbed NO<sub>x</sub> species have been reported to block the active sites for O2 activation in NH3 oxidation, leading to loss of activity. [32] This is consistent with the kinetics of the fresh CuO-Fe<sub>2</sub>O<sub>3</sub> catalyst (Figure 3d). Competitive adsorption experiments of NH<sub>3</sub>, O<sub>2</sub> and NO over the fresh catalyst and the ball-milled catalyst were conducted at room temperature (Figure S24). For the surface Cu SAC, the adsorbed NO (Figure S25) is not desorbed under ultra-high vacuum (UHV) and is not replaced by NH<sub>3</sub> (Figure S26) and O<sub>2</sub> (Figure S27). However, the adsorbed NH<sub>3</sub> is desorbed under UHV. For the subsurface Cu SAC, both the adsorbed NO and NH3 were desorbed under UHV. Subsequent desorption experiments were conducted from room temperature (RT) to 573 K. NO was adsorbed on the catalyst at RT and the desorption of surface species was monitored with the raising of temperature from RT to 573 K (Figure S28). The adsorbed N species disappeared quickly over the subsurface Cu SAC catalyst, while the peaks for adsorbed N species were stable even under 573 K over the surface Cu SAC (Figure 3e). These results indicate that the surface Cu species play an important role in NO adsorption, which agrees with DFT calculations (Figure S29 and Table S2).

To further prove the different adsorption behaviours of surface Cu and subsurface Cu, valence-to-core  $(K\beta_{2.5})$  X-ray emission spectroscopy (VtC-XES) was measured under different conditions. Recognizable changes were still observed under different atmospheres. The most significant difference was the intensity of the peak of the two catalysts (Figure 3f). The Cu in fresh catalyst has higher  $K\beta_{25}$ intensity under NH<sub>3</sub> and NH<sub>3</sub>+NO conditions, while the spectra of Cu in the subsurface are similar in different environments (Figure S30). These results further indicate that the surface Cu can coordinate with N, while the subsurface Cu can hardly coordinate with N during the reaction. The in situ XES results are consistent with the NAP-NEXAFS results. The strong adsorption of NO on catalysts may cause deactivation because of the loss of active sites for NH<sub>3</sub> and O<sub>2</sub> adsorption. High resilience to NO poisoning of ball-milled catalyst is attributed to durable single Cu atoms in the Fe<sub>2</sub>O<sub>3</sub> subsurface.

In situ diffuse reflectance Fourier transform spectrometry (DRIFTS) was used to explore the reaction intermediates of different catalysts. The co-introduction of NH $_3$  and O $_2$  was recorded for surface and subsurface Cu SACs from 473 K to 573 K, as shown in Figure 4.

The co-introduction of NH<sub>3</sub> and O<sub>2</sub> was recorded for surface and subsurface Cu SACs from 473 K to 573 K, as shown in Figure 4. The bands at 1140 and 1404 cm<sup>-1</sup> on the surface Cu SAC can be assigned to ammonia species bound to Lewis acid sites<sup>[33]</sup> and Brønsted acid sites,<sup>[34]</sup> respectively.



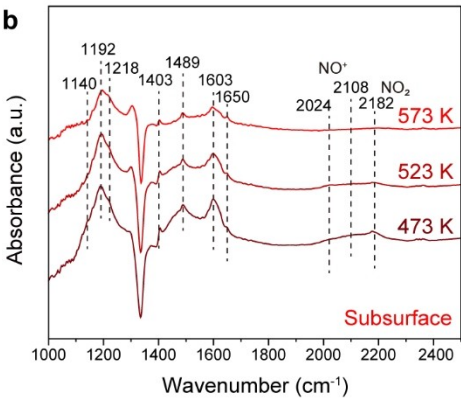


Figure 4. In situ DRIFTS study. In situ DRIFT spectra of  $NH_3$  oxidation over (a) 1 wt%  $CuO-Fe_2O_3$  (fresh, surface Cu SAC) and (b) 1 wt%  $CuO-Fe_2O_3$  (ball milling, subsurface Cu SAC) at 473 K, 523 K and 573 K. Feed: 5000 ppm  $NH_3$ , 5%  $O_2$ , He as balance.

The band at 1902 cm<sup>-1</sup> could be ascribed to the adsorbed NO species, [35] while such a band cannot be detected on the surface of the subsurface Cu SAC. The monodentate nitrate<sup>[36]</sup> (1243 and 1470 cm<sup>-1</sup>) and bridging nitrate<sup>[37]</sup> (1613 cm<sup>-1</sup>) species were observed on the surface Cu–Fe<sub>2</sub>O<sub>3</sub> catalyst, whereas no such bands emerged on the subsurface Cu-Fe<sub>2</sub>O<sub>3</sub> catalyst. In the i-SCR mechanism, nitrate species often regarded as representative reaction are intermediates. [38] In this mechanism, NH3 undergoes oxidation, leading to the formation of various types of nitrates, which subsequently engage in SCR reaction pathways by reacting with NH<sub>3</sub>. The absence of nitrate and nitrite species indicates that the subsurface Cu SAC did not follow the conventional i-SCR mechanism. For subsurface Cu SAC, the bands at 1403, 1489 and 1650 cm<sup>-1</sup> were assigned to adsorbed NH<sub>4</sub><sup>+</sup> on Brønsted acid sites, [39] while the bands at 1140, 1192, 1218 and  $1603\,\mathrm{cm^{-1}}$  were ascribed to  $NH_3$ adsorbed on the Lewis acid sites. [40]

The bands observed at 2024 and  $2108\,\mathrm{cm^{-1}}$  on both catalysts were attributed to  $\mathrm{NO^{+}}$  species adsorbed on various cationic positions. [41] The bands at  $2182\,\mathrm{cm^{-1}}$  could be assigned to adsorbed  $\mathrm{NO_{2}}$ , [42] which was consumed at elevated temperatures for both catalysts. Such consumable -NO<sub>2</sub> indicates the occurrence of the fast i-SCR mechanism, [43] wherein  $\mathrm{NO_{2}}$  further reacts with ammonia to form  $\mathrm{N_{2}}$  and  $\mathrm{H_{2}O}$ , as demonstrated below:

Angewandte

 $2NH_3 + NO + NO_2 \rightarrow 2N_2 + 3H_2O$ 

Recently, Lan et al.<sup>[44]</sup> reported that the limited selective oxidation of NH<sub>3</sub> into N<sub>2</sub> over CuO/Al<sub>2</sub>O<sub>3</sub> was attributed to the poor adsorption and activation of reactants, which is due to the strong adsorption of intermediates on conventional CuO sites. The accumulations of NO<sup>+</sup> intermediates were observed on the surface Cu SAC, while the adsorbed -NO<sub>2</sub> was consumed at 573 K. This observation indicates the limited O<sub>2</sub> activation of the surface Cu SAC, which could only oxidize the adsorbed NH<sub>3</sub> into –NOx intermediates rather than facilitate the subsequent fast i-SCR reaction. In contrast, NO<sup>+</sup> species are not observed for the subsurface Cu SAC at 573 K (Figure 4b), indicating the fast transformation from NO<sup>+</sup> species to other species. The poison effect of NO over the surface Cu SAC agrees well with the NAP-NEXAFS and VtC-XES results.

Liu et al. [45] found that the rapid depletion and replenishment of lattice oxygen facilitated the transformation of NO+ species and the formation of N<sub>2</sub>. Combining in situ experiments, the subsurface Cu SAC showed better redox performance of Fe<sub>2</sub>O<sub>3</sub> and weak adsorption of intermediates, leading to higher activity in NH<sub>3</sub>–SCO. As for the surface Cu SAC, the formation of monodentate nitrate and the consumption of –NO<sub>2</sub> adsorbed species under high temperatures indicated that the NH<sub>3</sub>-SCO reaction was guided by the i-SCR mechanism and the fast i-SCR mechanism. However, the fast i-SCR mechanism was limited by the weak O<sub>2</sub> activation capacity over surface Cu SAC.

To better understand the important role of subsurface Cu, we also performed in situ DRIFTS measurements for the Fe<sub>2</sub>O<sub>3</sub> support (Figure S31). The bands at 1192 and 1357 cm<sup>-1</sup> on the surface of Fe<sub>2</sub>O<sub>3</sub> can be assigned to ammonia species bound to Lewis acid sites. The monodentate nitrate [36] (1243, 1470 and 1546 cm<sup>-1</sup>) and bridging nitrate [37] (1613 cm<sup>-1</sup>) species were observed on the surface Fe<sub>2</sub>O<sub>3</sub> supports, suggesting that the NH<sub>3</sub>-SCO on Fe<sub>2</sub>O<sub>3</sub> follows the conventional i-SCR mechanism.

The bands observed at 2210 and 2238 cm $^{-1}$  on Fe<sub>2</sub>O<sub>3</sub> supports were attributed to N<sub>2</sub>O species. However, the adsorbed NO $^+$  species and adsorbed NO<sub>2</sub> cannot be observed. These results suggest the Fe<sub>2</sub>O<sub>3</sub> supports have restricted O<sub>2</sub> activation but suffer from the formation of N<sub>2</sub>O. These findings highlight the efferct of the ball milling to modify the surface of the catalysts and enhance the catalytic performance.

Isolated single metal atoms are usually anchored on the surface of metal oxides by strong metal-support interactions. [3a,46] However, these anchoring strategies may not be effective for reactions at high temperatures, especially in harsh reaction environments. [10a,47] Fe<sub>2</sub>O<sub>3</sub> was reported to have a much higher Tammann temperature (around 1400 K) than Cu, [48] and it can act as an inhibitor to prevent the sintering of subsurface Cu atoms. To explore the structural change of the catalyst, the measurement by a HAADF-STEM of the sample after the reaction was performed. As shown in Figure S32, Fe<sub>2</sub>O<sub>3</sub> nanoparticles were still remained similar in particle size, which indicated

that  $\text{Fe}_2\text{O}_3$  could not sinter significantly to cause severe deactivation.

To investigate the chemical state of Cu during the reaction, the high-energy-resolution fluorescence detected X-ray absorption near edge structure (HERFD-XANES) were measured under different conditions. The Cu in the fresh catalyst was in the form of Cu<sup>2+</sup> from room temperature to 573 K under NH<sub>3</sub> oxidation conditions. The catalyst after ball milling shows a pre-edge peak at 8983 eV, which has been reported to be due to a transition from a 1s to the doubly degenerate 4pxy orbitals in a two-coordinate Cu+ system. [49] This feature can exist under 473 K and Cu<sup>+</sup> can be oxidized to Cu<sup>2+</sup> at 573 K (Figure S33). The HERFD-XANES spectra of Cu<sup>2+</sup> in the subsurface show higher white line amplitudes than that of Cu2+ on the surface, suggesting different coordination environments of Cu (Figure 5a). To further verify the DFT model, we simulated the Cu K-edge XANES spectra with different Cu locations. For Cu on the surface of Fe<sub>2</sub>O<sub>3</sub>, the Cu K-edge XANES shows lower white line amplitudes compared with Cu in the subsurface (Figure S34), which is in line with the experimental XANES spectra.

Changes in the oxidation state of Cu as well as in the near edge structures were observed for the sample under different conditions at 573 K (Figure 5a–c). NH<sub>3</sub> and NH<sub>3</sub>+ NO in sequence provide a reduction atmosphere for Cu as expected. Cu in the fresh catalyst is easier to be reduced and can be reduced to Cu<sup>0</sup> cluster, while Cu in the ball-milled catalyst is more stable and even cannot be fully reduced to Cu<sup>+</sup> (Figure 5b). Under the reduction conditions (NH<sub>3</sub>+ NO), the surface Cu single atoms sintered, but subsurface Cu species were still anchored as single atoms in the catalyst subsurface. Cu was then fully oxidized to Cu<sup>2+</sup> in NO+O<sub>2</sub> for both catalysts. The reduction and oxidation of subsurface Cu can also be observed in NAP-NEXAFS (Figure S35), which suggests a facile subsurface diffusion of O vacancies around impurity atoms, <sup>[50]</sup> enhancing catalytic activities. <sup>[51]</sup>

The different stability between the two catalysts can also be shown after continuous reduction and oxidation. After a reduction in NH<sub>3</sub>+NO and oxidation in NO+O<sub>2</sub>, the fresh catalyst shows an obvious shoulder, which is similar to the CuO standard (Figure S36), while the Cu coordination environment of the ball-milled catalyst remained unchanged (Figure 5c). Based on our XANES results of Cu single atoms and clusters, [19-20] the absorption energies for the 1s-4p<sub>z</sub> (i.e., the shakedown peak from ligand-to-metal charge transfer) and  $1s\rightarrow 4p_{xy}$  transition rise with less CuO loading. For subsurface Cu single atoms in Fe<sub>2</sub>O<sub>3</sub>, this phenomenon can also be observed (as shown in Figure S37). For Cu single atoms on the surface and in the subsurface, the transition energies of  $1s\rightarrow 4p_z$  are 8986.4 eV and 8987.0 eV (Table S3), respectively. The higher 1s-4pz transition energy suggests that the electron-withdrawing effect is strengthened by increasing the number of Fe3+ ions per Cu site for subsurface Cu SACs. The absorption energies for the  $1s\rightarrow 4p_z$  and  $1s\rightarrow 4p_{xy}$  transition decrease (2.3 eV and 0.7 eV, Table S3) for the surface single-atom catalyst after reduction and oxidation. In contrast, the  $1s\rightarrow 4p_z$  and  $1s\rightarrow 4p_{xy}$  transition energies of subsurface single-atom catalyst are still higher

15213737, 2024, 42, Downloaded from https://onlinelibrary.wiley.com/doi/10.1002/ange.202140457 by University College London UCL Library Services, Wiley Online Library on [1003/2025], See the Terms and Conditions (https://onlinelibrary.wiley.com/erms-and-conditions) on Wiley Online Library for rules of use, OA articles are governed by the applicable Centwise.

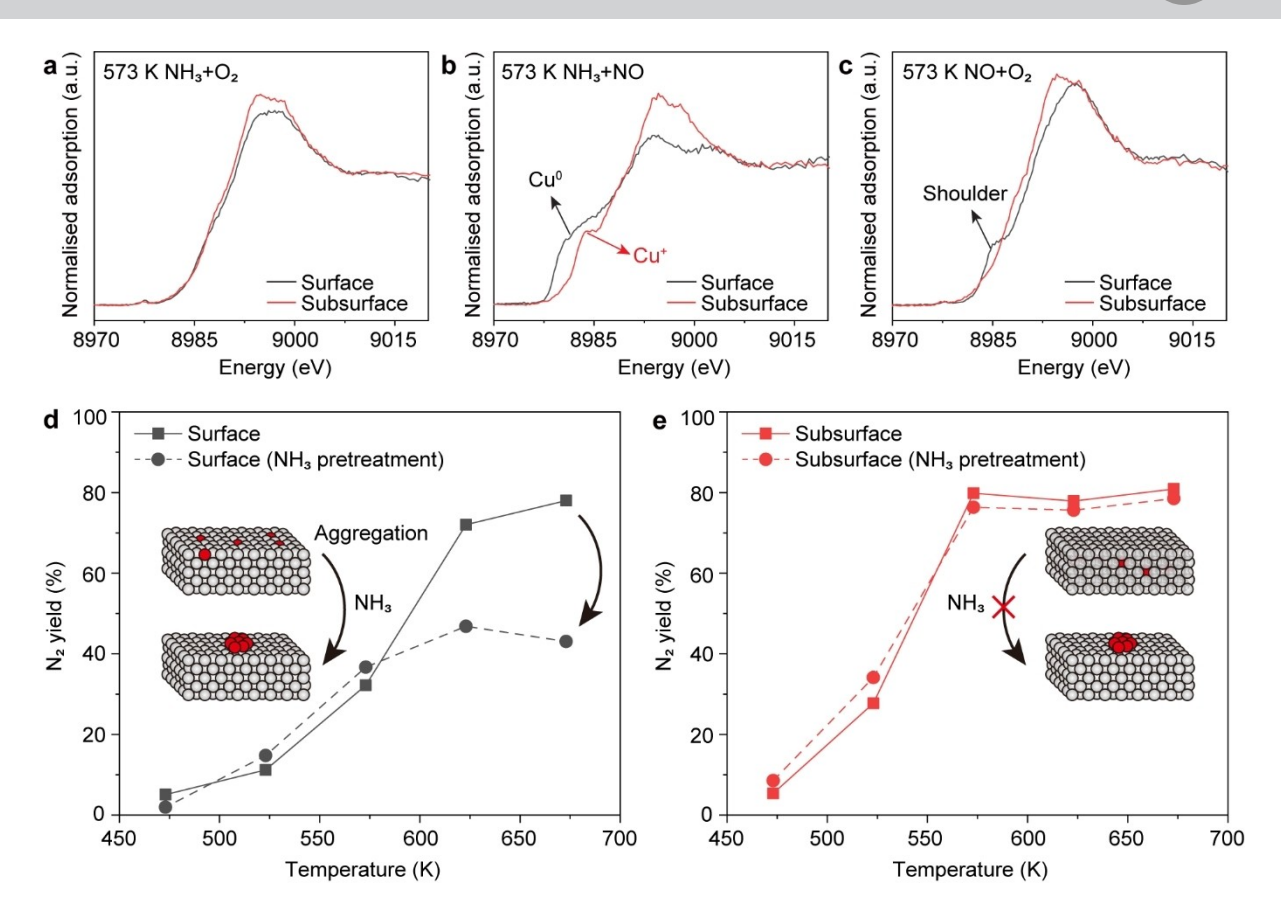


Figure 5. Evaluation of stability under reduction conditions. Cu HERFD-XANES spectra of 1 wt% CuO—Fe<sub>2</sub>O<sub>3</sub> (fresh, surface Cu SAC) and 1 wt% CuO—Fe<sub>2</sub>O<sub>3</sub> (ball milling, subsurface Cu SAC) samples in (a) NH<sub>3</sub> + O<sub>2</sub>, (b) NH<sub>3</sub> + NO and (c) NO + O<sub>2</sub> under 573 K. d, N<sub>2</sub> yield of 1 wt% CuO—Fe<sub>2</sub>O<sub>3</sub> (fresh, surface Cu SAC) before and after NH<sub>3</sub> pre-treatment. e, N<sub>2</sub> yield of 1 wt% CuO—Fe<sub>2</sub>O<sub>3</sub> (ball milling, subsurface Cu SAC) before and after NH<sub>3</sub> pre-treatment.

than that of CuO (Figure S37). The decrease of  $1s\rightarrow 4p_z$  and  $1s\rightarrow 4p_{xy}$  energies suggests the formation of CuO clusters for Cu single atoms over Fe<sub>2</sub>O<sub>3</sub> after reduction and oxidation.

The operando XAFS experiments show similar results in NH<sub>3</sub> oxidation conditions under high WHSV (Figure S38). The surface Cu single atoms keep in the form of Cu<sup>2+</sup>, while the small amount of Cu<sup>+</sup> in the subsurface single-atom catalyst gradually oxidised with the increase of temperature. In agreement with HERFD-XANES results, the operando XANES experiments exhibited a higher white line amplitude for subsurface Cu SACs (Figure S39). The reducing treatment, such as NH<sub>3</sub>, causes the formation of Cu<sup>0</sup> clusters for surface Cu single-atom catalysts (Figure S39). In comparison, Cu in the subsurface can only be partially reduced to Cu<sup>+</sup>. The oxidation and reduction of subsurface Cu suggest that Cu can activate the lattice O in Fe<sub>2</sub>O<sub>3</sub>, thereby improving the redox behaviour of Fe<sub>2</sub>O<sub>3</sub>. The sintering of surface Cu single atoms leads to substantially decreases N<sub>2</sub> yields (Figure 5d), while subsurface Cu single atoms show robustness under both oxidative (Figure S40) and reductive environments (Figure 5e).

These results suggest that the subsurface single atoms with less mobility are well resistant to sintering.

We found that the electronic structure of subsurface Cu single atoms shows no obvious change after reduction and

oxidation (Figure S37b,d). In contrast, surface Cu sintered after reduction and oxidation, showing similar transition energy of  $1s\rightarrow 4p_z$  and  $1s\rightarrow 4p_{xy}$  with the CuO standard (Figure S37a,c). The significant agglomeration of surface Cu caused severe deactivation in  $N_2$  productivity (Figure 5d), while subsurface Cu SAC kept the catalytic performance after reduction (Figure 5e). Therefore, both the morphology of catalysts and environment coordination of the subsurface Cu species remain unchanged after the reaction.

#### Conclusion

These observations illustrate the value of the subsurface single-atom catalysts design strategy, which opens promising perspectives to initiate the lattice distortion and facilitate the activation of the inactive lattice oxygen. The mechanochemical approach has been shown to be an effective method of regulating the position of single atoms. Controlling single atoms at the surface or subsurface results in catalysts with very different adsorption properties, leading to different reaction mechanisms. Such nanoengineering of SAC provides new ideas for preventing the poisoning of SAC and for designing different reaction pathways. For practical applications, the subsurface Cu single atoms in



 $Fe_2O_3$  remained isolated under either oxidation or reduction environments, while surface Cu single atoms on  $Fe_2O_3$  sintered under reduction. Our findings for immersing single metal atoms in the subsurface of supports constitute a promising new target for the development of advanced metal catalysts in oxidation chemistry.

# Acknowledgements

The project is funded by EPSRC (EP/P02467X/1 and EP/ S018204/2), Royal Society (RG160661, IES\R3\170097, IES \R1\191035 and IEC\R3\193038) and RS-JSPS funding. We acknowledge electron Physical Science Imaging Centre at Diamond Light Source (DLS, UK) for the STEM experiment (Proposal No. MG23759 and MG24450). We acknowledge the Diamond Light Source for time on beamtime B07-C under proposal SI29094. We acknowledge the Diamond Light Source beamtime at I20-Scanning under proposal SP29092. We acknowledge the Diamond Light Source for beamtime at I09 under proposal SI31852 and Pardeep Kumar Thakur for support. We acknowledge SPring-8 for the XAFS experiments conducted under proposal no. 2021A1695. We acknowledge Helmholz-Zentrum Berlin for the beamtime in BESSY II (221-10847ST). We thank Dr Hrishikesh Joshi for his help during sample synthesis We acknowledge the UK Catalysis Hub for resources and support provided and thank Dr June Callison and Dr Donato Decarolis for their help for in situ DRIFTS experiments. X.G. would like to thank the China Scholarship Council (CSC) for the PhD funding.

### **Conflict of Interest**

The authors declare no conflict of interest.

## **Data Availability Statement**

The data that support the findings of this study are available in the supplementary material of this article.

 $\textbf{Keywords:} \ \ \text{single-atom catalysts} \cdot \text{ammonia oxidation} \cdot \text{ball} \\ \text{milling} \cdot \text{surface chemistry} \cdot \text{heterogeneous catalysis} \\$ 

- [1] B. Qiao, A. Wang, X. Yang, L. F. Allard, Z. Jiang, Y. Cui, J. Liu, J. Li, T. Zhang, *Nat. Chem.* **2011**, *3*, 634–641.
- [2] a) R. Lang, X. R. Du, Y. K. Huang, X. Z. Jiang, Q. Zhang, Y. L. Guo, K. P. Liu, B. T. Qiao, A. Q. Wang, T. Zhang, Chem. Rev. 2020, 120, 11986–12043; b) J. J. Li, Q. Q. Guan, H. Wu, W. Liu, Y. Lin, Z. H. Sun, X. X. Ye, X. S. Zheng, H. B. Pan, J. F. Zhu, S. Chen, W. H. Zhang, S. Q. Wei, J. L. Lu, J. Am. Chem. Soc. 2019, 141, 14515–14519; c) H. Zhao, R. Yu, S. Ma, K. Xu, Y. Chen, K. Jiang, Y. Fang, C. Zhu, X. Liu, Y. Tang, L. Wu, Y. Wu, Q. Jiang, P. He, Z. Liu, L. Tan, Nat. Catal. 2022, 5, 818–831
- [3] a) Z. Zhang, Y. Zhu, H. Asakura, B. Zhang, J. Zhang, M. Zhou, Y. Han, T. Tanaka, A. Wang, T. Zhang, N. Yan, Nat.

- Commun. 2017, 8, 16100; b) L. Nie, D. Mei, H. Xiong, B. Peng, Z. Ren, X. I. P. Hernandez, A. DeLaRiva, M. Wang, M. H. Engelhard, L. Kovarik, A. K. Datye, Y. Wang, Science 2017, 358, 1419–1423.
- [4] H. Li, L. Wang, Y. Dai, Z. Pu, Z. Lao, Y. Chen, M. Wang, X. Zheng, J. Zhu, W. Zhang, R. Si, C. Ma, J. Zeng, *Nat. Nanotechnol.* 2018, 13, 411–417.
- [5] Y. Yao, Z. Huang, P. Xie, L. Wu, L. Ma, T. Li, Z. Pang, M. Jiao, Z. Liang, J. Gao, Y. He, D. J. Kline, M. R. Zachariah, C. Wang, J. Lu, T. Wu, T. Li, C. Wang, R. Shahbazian-Yassar, L. Hu, Nat. Nanotechnol. 2019, 14, 851–857.
- [6] J. Gu, C.-S. Hsu, L. Bai, H. M. Chen, X. Hu, Science 2019, 364, 1091–1094.
- [7] D. Liu, X. Li, S. Chen, H. Yan, C. Wang, C. Wu, Y. A. Haleem, S. Duan, J. Lu, B. Ge, P. M. Ajayan, Y. Luo, J. Jiang, L. Song, *Nat. Energy* 2019, 4, 512–518.
- [8] B.-H. Lee, S. Park, M. Kim, A. K. Sinha, S. C. Lee, E. Jung, W. J. Chang, K.-S. Lee, J. H. Kim, S.-P. Cho, H. Kim, K. T. Nam, T. Hyeon, *Nat. Mater.* 2019, 18, 620–626.
- [9] a) L. DeRita, J. Resasco, S. Dai, A. Boubnov, H. V. Thang, A. S. Hoffman, I. Ro, G. W. Graham, S. R. Bare, G. Pacchioni, X. Pan, P. Christopher, *Nat. Mater.* 2019, 18, 746–751; b) F. Maurer, J. Jelic, J. Wang, A. Gänzler, P. Dolcet, C. Wöll, Y. Wang, F. Studt, M. Casapu, J.-D. Grunwaldt, *Nat. Catal.* 2020, 3, 824–833.
- [10] a) S. Duan, R. Wang, J. Liu, *Nanotechnology* 2018, 29, 204002;
  b) X. Li, X. I. Pereira-Hernández, Y. Chen, J. Xu, J. Zhao, C.-W. Pao, C.-Y. Fang, J. Zeng, Y. Wang, B. C. Gates, J. Liu, *Nature* 2022, 611, 284–288;
  c) V. Muravev, G. Spezzati, Y.-Q. Su, A. Parastaev, F.-K. Chiang, A. Longo, C. Escudero, N. Kosinov, E. J. M. Hensen, *Nat. Catal.* 2021, 4, 469–478.
- [11] a) J. Liu, F. R. Lucci, M. Yang, S. Lee, M. D. Marcinkowski, A. J. Therrien, C. T. Williams, E. C. H. Sykes, M. Flytzani-Stephanopoulos, J. Am. Chem. Soc. 2016, 138, 6396–6399; b) L. Cao, W. Liu, Q. Luo, R. Yin, B. Wang, J. Weissenrieder, M. Soldemo, H. Yan, Y. Lin, Z. Sun, C. Ma, W. Zhang, S. Chen, H. Wang, Q. Guan, T. Yao, S. Wei, J. Yang, J. Lu, Nature 2019, 565, 631–635.
- [12] J. Becher, D. F. Sanchez, D. E. Doronkin, D. Zengel, D. M. Meira, S. Pascarelli, J.-D. Grunwaldt, T. L. Sheppard, *Nat. Catal.* 2021, 4, 46–53.
- [13] M. Jablonska, A. M. Beale, M. Nocun, R. Palkovits, Appl. Catal. B 2018, 232, 275–287.
- [14] D. P. Nolan, in Fire Pump Arrangements at Industrial Facilities (Third Edition) (Ed.: D. P. Nolan), Gulf Professional Publishing 2017, pp. 161–167.
- [15] F. Y. Gao, Y. Y. Liu, Z. Sani, X. L. Tang, H. H. Yi, S. Z. Zhao, Q. J. Yu, Y. S. Zhou, J. Environ. Chem. Eng. 2021, 9, 104575.
- [16] D. A. Svintsitskiy, L. S. Kibis, A. I. Stadnichenko, E. M. Slavinskaya, A. V. Romanenko, E. A. Fedorova, O. A. Stonkus, D. E. Doronkin, V. Marchuk, A. Zimina, M. Casapu, J. D. Grunwaldt, A. I. Boronin, *ChemCatChem* 2020, 12, 867–880.
- [17] a) M. Jablonska, R. Palkovits, Appl. Catal. B 2016, 181, 332–351; b) X. Guan, H. Asakura, R. Han, S. Xu, H.-X. Liu, L. Chen, Z. Yao, J. H. C. Yan, T. Tanaka, Y. Guo, C.-J. Jia, F. R. Wang, ACS Catal. 2023, 13816–13827.
- [18] a) W. Chen, S. Yang, H. Liu, F. Huang, Q. Shao, L. Liu, J. Sun, C. Sun, D. Chen, L. Dong, *Environ. Sci. Technol.* 2022, 56, 10442–10453; b) F. Liu, W. Shan, Z. Lian, J. Liu, H. He, *Appl. Catal. B* 2018, 230, 165–176.
- [19] L. Kang, B. Wang, Q. Bing, M. Zalibera, R. Büchel, R. Xu, Q. Wang, Y. Liu, D. Gianolio, C. C. Tang, E. K. Gibson, M. Danaie, C. Allen, K. Wu, S. Marlow, L.-d. Sun, Q. He, S. Guan, A. Savitsky, J. J. Velasco-Vélez, J. Callison, C. W. M. Kay, S. E. Pratsinis, W. Lubitz, J.-y. Liu, F. R. Wang, Nat. Commun. 2020, 11, 4008.



5213757, 2024

, 42, Downloaded from https://onlinelibbary.wiley.com/doi/10.1002/ange.202410457 by University College London UCL Library Services, Wiley Online Library on [1003/2025]. See the Terms and Conditions (https://onlinelibrary.wiley.com/errars-and-conditions) on Wiley Online Library for rules of use; OA articles are governed by the applicable Creative Commonsory.

- [20] X. Guan, R. Han, H. Asakura, Z. Wang, S. Xu, B. Wang, L. Kang, Y. Liu, S. Marlow, T. Tanaka, Y. Guo, F. R. Wang, ACS Catal. 2022, 15207–15217.
- [21] a) J. De Bellis, H. Petersen, J. Ternieden, N. Pfänder, C. Weidenthaler, F. Schüth, Angew. Chem. Int. Ed. 2022, 61, e202208016; b) J. De Bellis, C. Ochoa-Hernández, C. Farès, H. Petersen, J. Ternieden, C. Weidenthaler, A. P. Amrute, F. Schüth, J. Am. Chem. Soc. 2022, 144, 9421–9433.
- [22] M. Munoz, P. Argoul, F. Farges, Am. Mineral. 2003, 88, 694– 700
- [23] a) S. Tanuma, C. J. Powell, D. R. Penn, Surf. Interface Anal. 1988, 11, 577–589; b) S. Tanuma, C. Powell, D. Penn, Surf. Interface Anal. 2003, 35, 268–275.
- [24] a) F. Lin, I. M. Markus, D. Nordlund, T. C. Weng, M. D. Asta, H. L. L. Xin, M. M. Doeff, Nat. Commun. 2014, 5; b) J.-P. Deville, C. S. Cojocaru, in Materials Surface Processing by Directed Energy Techniques (Ed.: Y. Pauleau), Elsevier, Oxford 2006, pp. 411–441.
- [25] a) H. Idriss, Surf. Sci. 2021, 712, 121894; b) S.-S. Li, W.-J. Li, T.-J. Jiang, Z.-G. Liu, X. Chen, H.-P. Cong, J.-H. Liu, Y.-Y. Huang, L.-N. Li, X.-J. Huang, Anal. Chem. 2016, 88, 906–914.
- [26] a) A. D. Allian, K. Takanabe, K. L. Fujdala, X. Hao, T. J. Truex, J. Cai, C. Buda, M. Neurock, E. Iglesia, J. Am. Chem. Soc. 2011, 133, 4498–4517; b) M. Cargnello, V. V. T. Doan-Nguyen, T. R. Gordon, R. E. Diaz, E. A. Stach, R. J. Gorte, P. Fornasiero, C. B. Murray, Science 2013, 341, 771–773.
- [27] a) Y. Lu, J. Wang, L. Yu, L. Kovarik, X. Zhang, A. S. Hoffman, A. Gallo, S. R. Bare, D. Sokaras, T. Kroll, V. Dagle, H. Xin, A. M. Karim, *Nat. Catal.* 2019, 2, 149–156; b) W.-Z. Yu, W.-W. Wang, S.-Q. Li, X.-P. Fu, X. Wang, K. Wu, R. Si, C. Ma, C.-J. Jia, C.-H. Yan, *J. Am. Chem. Soc.* 2019, *141*, 17548–17557
- [28] a) M.-H. Liu, Y.-W. Chen, T.-S. Lin, C.-Y. Mou, ACS Catal. 2018, 8, 6862–6869; b) L. DeRita, S. Dai, K. Lopez-Zepeda, N. Pham, G. W. Graham, X. Pan, P. Christopher, J. Am. Chem. Soc. 2017, 139, 14150–14165.
- [29] A. Ruiz Puigdollers, P. Schlexer, S. Tosoni, G. Pacchioni, ACS Catal. 2017, 7, 6493–6513.
- [30] S. Giovannini, F. Boscherini, R. Carboni, L. Signorini, L. Pasquini, N. Mahne, A. Giglia, M. Pedio, S. Nannarone, M. Benfatto, S. Della Longa, *Phys. Scr.* 2005, 2005, 424.
- [31] S. H. Sun, H. Zeng, D. B. Robinson, S. Raoux, P. M. Rice, S. X. Wang, G. X. Li, J. Am. Chem. Soc. 2004, 126, 273–279.
- [32] L. Gang, B. G. Anderson, J. van Grondelle, R. A. van Santen, J. Catal. 2001, 199, 107–114.
- [33] Y. Zhang, J. Chen, Z. Liu, Catal. Today 2022, 402, 115–121.
- [34] a) Z. Hua, H. Song, C. Zhou, Q. Xin, F. Zhou, W. Fan, S. Liu, X. Zhang, C. Zheng, Y. Yang, X. Gao, *Chem. Eng. J.* 2023, 473, 145106; b) J. Huang, Z. Tong, Y. Huang, J. Zhang, *Appl. Catal. B* 2008, 78, 309–314.
- [35] a) H.-Y. Chen, M. Kollar, Z. Wei, F. Gao, Y. Wang, J. Szanyi, C. H. F. Peden, *Catal. Today* **2019**, *320*, 61–71; b) J. Szanyi, M. T. Paffett, *J. Catal.* **1996**, *164*, 232–245.

- [36] a) X. Xiao, J. Wang, X. Jia, C. Ma, W. Qiao, L. Ling, ACS Omega 2021, 6, 12801–12812; b) Y. Che, X. Liu, Z. Shen, K. Zhang, X. Hu, A. Chen, D. Zhang, Langmuir 2023, 39, 7434–7443.
- [37] L. Liu, Y. Cao, W. Sun, Z. Yao, B. Liu, F. Gao, L. Dong, *Catal. Today* 2011, 175, 48–54.
- [38] F. Wang, J. Z. Ma, G. Z. He, M. Chen, C. B. Zhang, H. He, ACS Catal. 2018, 8, 2670–2682.
- [39] Y. He, M. E. Ford, M. Zhu, Q. Liu, Z. Wu, I. E. Wachs, Appl. Catal. B 2016, 188, 123–133.
- [40] a) N. Y. Topsoe, H. Topsoe, J. A. Dumesic, J. Catal. 1995, 151, 226–240; b) Z. Liu, S. Zhang, J. Li, L. Ma, Appl. Catal. B 2014, 144, 90–95.
- [41] a) R. Kefirov, E. Ivanova, K. Hadjiivanov, S. Dzwigaj, M. Che, Catal. Lett. 2008, 125, 209–214; b) G. Li, S. C. Larsen, V. H. Grassian, J. Mol. Catal. A 2005, 227, 25–35.
- [42] G. Mul, M. W. Zandbergen, F. Kapteijn, J. A. Moulijn, J. Pérez-Ramírez, Catal. Lett. 2004, 93, 113–120.
- [43] T. Lan, J. Deng, X. Zhang, F. Wang, X. Liu, D. Cheng, D. Zhang, ACS Catal. 2022, 12, 3955–3964.
- [44] T. Lan, M. Gao, J.-y. Hasegawa, Y. Shen, W. Qu, Q. Hu, J. Deng, D. Cheng, D. Zhang, ACS Catal. 2023, 13, 14070–14079.
- [45] Y. Liu, Z. Liu, C. Wang, J. Xu, J. Ai, X. Liu, A. Zhang, Y. Zhao, C. Du, B. Shan, ACS Catal. 2023, 13, 7178–7188.
- [46] a) L. Lin, W. Zhou, R. Gao, S. Yao, X. Zhang, W. Xu, S. Zheng, Z. Jiang, Q. Yu, Y.-W. Li, C. Shi, X.-D. Wen, D. Ma, Nature 2017, 544, 80–83; b) J. Jones, H. F. Xiong, A. T. Delariva, E. J. Peterson, H. Pham, S. R. Challa, G. S. Qi, S. Oh, M. H. Wiebenga, X. I. P. Hernandez, Y. Wang, A. K. Datye, Science 2016, 353, 150–154.
- [47] a) C. Dessal, T. Len, F. Morfin, J.-L. Rousset, M. Aouine, P. Afanasiev, L. Piccolo, ACS Catal. 2019, 9, 5752–5759; b) C. Dessal, A. Sangnier, C. Chizallet, C. Dujardin, F. Morfin, J.-L. Rousset, M. Aouine, M. Bugnet, P. Afanasiev, L. Piccolo, Nanoscale 2019, 11, 6897–6904.
- [48] Y. Wang, J. Zhang, H. Jiang, C. Xu, Z. Liu, R. Xu, Z. Chen, Mater. Des. 2022, 215, 110434.
- [49] a) C. Paolucci, A. A. Verma, S. A. Bates, V. F. Kispersky, J. T. Miller, R. Gounder, W. N. Delgass, F. H. Ribeiro, W. F. Schneider, *Angew. Chem. Int. Ed.* 2014, 53, 11828–11833; b) T. V. W. Janssens, H. Falsig, L. F. Lundegaard, P. N. R. Vennestrom, S. B. Rasmussen, P. G. Moses, F. Giordanino, E. Borfecchia, K. A. Lomachenko, C. Lamberti, S. Bordiga, A. Godiksen, S. Mossin, P. Beato, *ACS Catal.* 2015, 5, 2832–2845.
- [50] Z. Łodziana, J. Piechota, Phys. Rev. B 2006, 74, 184117.
- [51] J. Kang, Y. Zhang, Z. Chai, X. Qiu, X. Cao, P. Zhang, G. Teobaldi, L.-M. Liu, L. Guo, Adv. Mater. 2021, 33, 2100407.

Manuscript received: June 3, 2024 Accepted manuscript online: July 14, 2024 Version of record online: September 5, 2024